MnO_x-based electrocatalysts for enhanced oxygen reduction in microbial fuel cell air cathodes

Fatemeh Shahbazi Farahani[1,2] , Barbara Mecheri [2,*] , Mir Reza Majidi [1,*], Maida Aysla Costa de Oliveira [2], Alessandra D'Epifanio [2], Francesca Zurlo [2], Ernesto Placidi [3,4], Fabrizio Arciprete [3], Silvia Licoccia [2]

1 Dept. of Analytical Chemistry, Faculty of Chemistry, University of Tabriz, 51664 Tabriz, Iran

2 Dept. of Chemical Science and Technologies, University of Rome Tor Vergata, Via della Ricerca Scientifica, 00133 Rome, Italy

3 Dept. of Physics, University of Rome Tor Vergata, Via della Ricerca Scientifica, 00133 Rome, Italy

4 CNR-ISM, Via Fosso del Cavaliere 100, Rome, Italy

*Corresponding authors

Barbara Mecheri

e-mail: barbara.mecheri@uniroma2.it; tel: +39 06 7259 4488

Mir Reza Majidi

email: majidi@tabrizu.ac.ir

tel: +98-413-335-5998

Abstract

Multivalent MnO_x supported on nitrogen-doped carbon (C(N)/MnO_x-SP) and reduced graphene oxide (rGO(N)/MnO_x-SP) is fabricated via a solid state method. The synthesized catalysts are characterized by X-ray diffraction (XRD), Raman spectroscopy, field emission scanning electron microscopy (FE-SEM), and X-ray photoelectron spectroscopy (XPS) to get insights on crystalline structure, morphology and surface chemistry. The electrocatalytic activity toward oxygen reduction reaction (ORR) is evaluated by cyclic voltammetry, hydrodynamic voltammetry with rotating disk electrode, and electrochemical impedance spectroscopy in neutral media. As compared to rGO(N)/MnO_x-SP, C(N)/ MnO_x-SP shows higher performance toward ORR, due to the interplay of surface chemistry and morphology. C(N)/MnO_x-SP is assembled as cathode of a single-chamber microbial fuel cell (MFC) fed with sodium acetate as fuel. The MFC performance is evaluated by measuring power generation and acquiring voltage generation cycles in long-term operation mode. MFCs assembled with C(N)/ MnO_x-SP exhibits a peak power density of 467 mWm^{-2}, slightly higher than that of reference Pt/C (446 mWm^{-2}). The obtained results indicate that C(N)/ MnO_x-SP is a viable catalyst for MFC cathodes owing competitive price and high performance in terms of power generation and stability of voltage cycle.

Keywords: Manganese dioxide, nitrogen-doped carbon, oxygen reduction reaction, air cathode, microbial fuel cell

1 Introduction

Microbial fuel cell (MFC) is a bioelectrochemical system which has attracted increasing attention during the past decade since it converts chemical energy stored in organic compounds to electrical power and simultaneously treats wastewater (1-3). However, the widespread diffusion of MFCs is constrained because of durability issues and high cost of materials, mainly arising from the use of platinum as catalyst for the oxygen reduction reaction (ORR) occurring at the cathode side.

A viable approach for reducing costs, while enhancing ORR, is the use of platinum group metal (PGM) free catalysts. Previous literature reports have shown that PGM-free catalysts obtained by supporting transition metal, such as Fe and Co, on different carbon supports can be used as cathode in MFCs, achieving an electrochemical performance comparable to that of Pt (4-8). Also, thanks to low cost, natural abundance, environmental friendly nature, and good electrochemical properties, electrode materials based on manganese dioxide (MnO_2) have been tested at the cathode side of MFCs (5, 6). ORR activity and the overall electrochemical performance was found to be strongly dependent on size, morphology, crystal structure, surface chemistry, and surface area (7-11).

MnO_2 can be synthesized following diverse strategies, including sol-gel process, microwave heating, and precipitation/ion-exchange, obtaining materials with different structure, surface area, and hydration degree (12-14). Generally, MnO_2 exists in three crystallographic forms, *i.e.* α-, β-, and γ-MnO_2, which correspond to differently connected [MnO_6] octahedral frameworks, resulting in different morphologies and pore structures (15-20).

However, MnO_2 has an intrinsic low electrical conductivity and suffers from agglomeration and dissolution issues, which limits its activity as ORR catalysts. Supporting MnO_2 on highly conductive materials, such as graphene and graphene oxide, carbon black, carbon nanotubes, and activated carbons is a widely recognized strategy for overcoming the above-mentioned drawbacks (21, 22).

Electronic conductivity, catalytic activity, and anchoring of the metal particles can be further enhanced by heteroatom functionalization of the carbon support (23-25). In particular, carbon materials show a nitrogen-doping-enhanced ORR activity in neutral and alkaline environment, due to improved adsorption of oxygen and decomposition of peroxide intermediate (26-30). In fact, there are two possible ways of oxygen reductions that can take place: oxygen can be reduced to water by direct 4-electron pathway or to peroxide by 2-electron pathway, following a pH-dependent mechanism as illustrated in Table 1. For achieving high power performance in MFCs and avoid peroxide formation, the direct 4-electron pathway is a mandatory requirement of ORR catalysts (28).

Table 1 ORR pathways and standard reduction potentials.

Reaction Mechanisms	Reaction	pH	**E^0(vs. SHE)**
4e pathway (direct)	$O_2 + 2H_2O + 4e^- \rightarrow 4OH^-$	alkaline	0.401 V
	$O_2 + 4H^+ + 4e- \rightarrow 2H_2O$	acidic	1.229 V
2e pathway (peroxide)	$O_2 + H_2O + 2e^- \rightarrow HO_2^- + OH^-$ $HO_2^- + H_2O + 2e^- \rightarrow 3OH^-$	alkaline	-0.065
	$O_2 + 2H^+ + 2e^- \rightarrow H_2O_2$ $H_2O_2 + 2H+ 2e^- \rightarrow 2\ H_2O$	acidic	0.670

Nitrogen-doping of carbon supports can be thus considered as an efficient way to improve MFC performance of previously reported MnO_2-based cathodes (31-36).

In this work, we report a strategy to develop a novel multivalent MnO_x supported on either nitrogen-doped carbon black or nitrogen-doped graphene oxide to be used at the cathode side of MFCs, for enhancing power generation, stability, and reducing costs. To the best of our knowledge, electrocatalysts based on multivalent MnO_x supported on N-doped carbon have not been yet investigated in air-cathode MFCs.

2 Experimental

2-1 Materials preparation

XC-72R Carbon Vulcan (C) was obtained by Cabot Corporation. It was modified by a two steps treatment with nitric acid and ammonia gas, according to previous reports (37) ,obtaining a material labeled as C(HNO_3) and C(N), respectively.

Graphene oxide was synthesized through electrochemical exfoliation of graphite in aqueous solution of LiCl, as previously reported (38). N-doping and reduction of GO was further carried out by a thermal treatment in a flow of anhydrous ammonia into a tubular oven at T= 400°C (heating rate of 5°C/min) for 4 h, obtaining a sample labeled as rGO(N).

MnO_x was supported on C(N) and rGO(N) by a solid state method. In a typical preparation, 4.16 mmol of either C(N) or rGO(N), 0.0416 mmol $Mn(Ac)_2{\cdot}4H_2O$, and 0.0277 mmol $KMnO_4$ (Mn^{+2}:Mn^{+7}=3:2) were mixed together in an agate mortar and ground for 20 minutes. The powder was then transferred to a glass vial, capped and kept at T=180°C for 8 hours. The resulting powder was cooled and thoroughly washed with distilled water and ethanol four times, and then dried at 60°C for 4 hours. Finally, the obtained samples were calcined at 400°C for 90 minutes, and labeled as C(N)/MnO_x-SP and rGO(N)/ MnO_x-SP, respectively.

2-2 Materials characterizations

To verify the crystalline structure, X-ray diffraction (XRD) was performed by using Philips PW1730 X-ray diffractometer with Cu K_α radiation (λ=1.5406 Å).

The morphology of the materials was investigated by scanning electron microscopy (SEM). All images were acquired using a Leo Supra 35 field-emission scanning electron microscope (Carl Zeiss, Oberkochen, Germany).

Raman Spectroscopy was performed with a DXR Raman Microscope (Thermo Scientific) using laser excitation wavelength of 532 nm with a 10 X objective. Laser power was maintained at 0.1 mW.

X-ray Photoelectron Spectroscopy (XPS) was performed using an Omicron DAR 400 Al/Mg Ka nonmonochromatized X-ray source, and a VG-CLAM2 electron spectrometer. Samples were dispersed in ethanol to a 1 $mgmL^{-1}$ content and deposited on silicon wafer.

The electrochemical tests to evaluate ORR activity of the different catalysts were carried out by Cyclic Voltammetry (CV), Electrochemical Impedance Spectroscopy (EIS), and Hydrodynamic Voltammetry with a Rotating Disc Electrode (RDE) model 636A (Princeton Applied Research, Ametek). All electrochemical tests were performed with a VMP3 Potentiostat (Bio Logic Science Instruments) connected to a computer through EC-lab V10.18 software. Fitting and analysis of the EIS data were done by ZView software. 100 mM neutral phosphate buffer (PBS) saturated with either nitrogen or oxygen was used as electrolyte. A three electrode cell was used, using saturated calomel electrode (Amel 303/SCG/12), Pt wire (Amel 805/SPG/6J) , and a glassy carbon disk (0.196 cm^2 area) modified with catalyst layer as the reference, counter, and working electrode, respectively. To prepare catalysts ink, 4 mg catalyst was dispersed in 455 µL of a mixture of ethanol, water and 5.0 wt% Nafion (Aldrich) with volume ratio 5.4:2.7:1. Then 7 µL of catalyst ink was deposited on the GC electrode to 0.31 $mgcm^{-2}$ catalyst loading.

CV experiments were performed in the potential range +1.1V ÷ -0.8 V (versus SCE) with scan rate in the range of 10-80 mVs^{-1}. Linear sweep voltammetry (LSV) with RDE electrodes was carried out at different rotation rates by sweeping the potential from -0.4 V ÷ -1 V (versus SCE) at 10 mVs^{-1}. EIS spectra were recorded at E= -0.3V and E=-0.6 V (vs. SCE) for C(N)/MnO_x-SP and rGO(N)/ MnO_x-SP, respectively, over a frequency range of 10 mHz to 100 kHz with an amplitude of 10 mV.

2-3 MFC operation:

2-3.1 Cathode preparation

In order to prepare modified carbon cloth cathodes, the diffusion layer (exposed to air) and the catalyst layer (faced to MFC solution) were applied and hot-pressed at pressure of 20 MPa and temperature of 120°C. 5 mg of the catalyst were dispersed in 0.83 µL DI water, 6.67 µL Nafion solution, and 3.33 µL 2-propanol and brush-painted on the surface of a mesoporous layer of a GDL carbon cloth (Quintech, Germany). The electrode was dried at room temperature for 24 h. On the opposite side, the diffusion layer was applied as previously described (37). A standard Pt/C cathode was prepared and taken as a reference for MFC testing. In both cases, the amount of either MnO_x or Pt loading was 0.5 $mgcm^{-2}$.

2-3.2 MFC tests

MFC tests were performed using lab-scale prototypes of single chamber air-cathode MFCs previously described. A two electrode configuration was used: the working electrode was connected to the cathode and the reference and the counter electrode were both connected to the anode, which is a graphite brush as previously reported (38, 39). MFCs were firstly acclimated and fed with phosphate buffer solution containing 1 gL^{-1} sodium acetate, acquiring voltage generation cycles (40). Polarization and power density curve were carried out by varying the external resistance (from 10-10000 Ω) every 30 minutes and measuring cell voltage at each resistance (41). All measurements were carried out at room temperature (23 ± 3 °C) having three independent replicates for each cathode.

3 Results and discussion

The morphology of C(N)/MnO_x-SP and rGO(N)/ MnO_x-SP was characterized by field emission scanning electron microscopy (FE-SEM) (Fig. 1). Depending on the preparation procedure, the sample morphology is very different. In fact, C(N)/MnO_x-SP (Fig. 1a) has a regular morphology, with the presence of homogeneous spherical particles and larger aggregates which are more evident at higher

magnification (Fig. 1b). In the case of rGO(N)/MnO_x-SP, the morphology is not as homogeneous as compared to C(N)/MnO_x-SP, showing a high degree of disorder (Fig. 1c). At higher magnification, it is possible to distinguish the lamellar shape of the carbon support from smaller and brighter round-shaped MnO_x nanoparticles (Fig. 1d). From SEM images, it is evident that MnO_x is more homogeneously distributed on C(N) rather than on rGO(N).

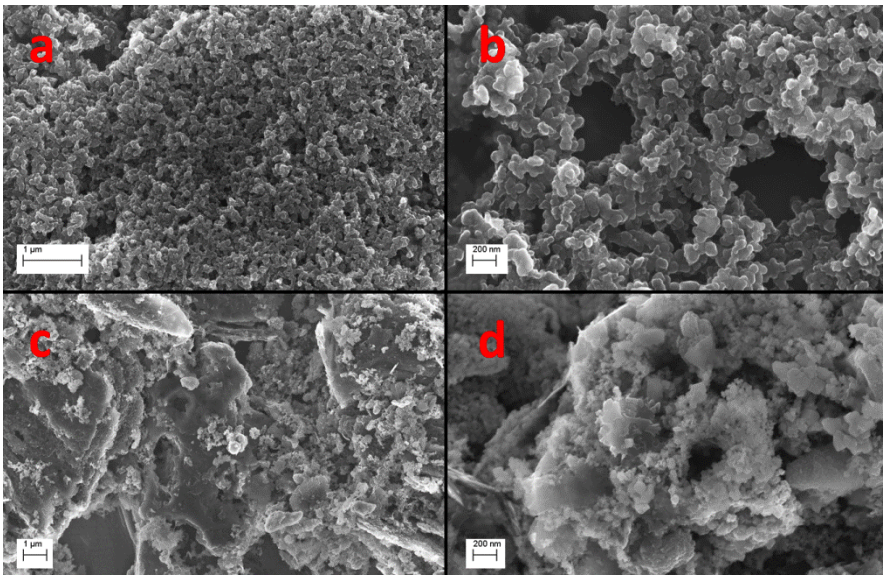

Figure 1- FE-SEM images of C(N)/ MnO_x-(SP) (a,b), rGO(N)/ MnO_x-SP (c,d).

The XRD patterns of MnO_x, C(N), C(N)/ MnO_x-SP, rGO(N), rGO(N)/ MnO_x-SP are shown in Fig.2, together with MnO_x peak identification according to JCPDS database. Fig. 2a shows the XRD pattern of bare MnO_x calcined at 400 °C, indicating the presence of diverse crystalline phases corresponding to the tetragonal structure of Mn_3O_4 (JCPDS No. 001-1127), MnO_2 (JCPDS No. 044-0141), Mn_2O_3 (JCPDS No. 024-0508), and MnO (JCPDS No. 075-1090). The presence of diverse crystalline phases can be ascribed to the low calcination temperature (400°C), resulting in a lack of energy for perfect crystallization. As previously reported (42-44), the calcination temperature has an effect on the formation of crystalline phases, in particular a higher calcination temperature leads to lower manganese valence, eventually affecting shape, texture, and particle size.

The diffraction pattern of C(N) in Fig. 2b shows a broad peak at 2θ=24° and two narrow peaks at 43° and 51°, which were assigned to typical features of N-doped carbon black. The XRD pattern of rGO(N) displays two narrow peaks at 2θ of 27° and 45° corresponding to the (002) and (101) planes, respectively.

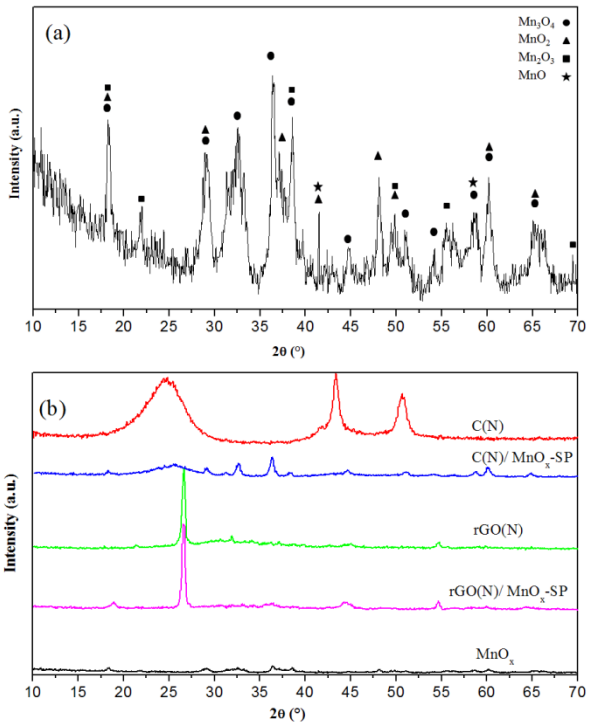

Figure 2- Identification of XRD peaks of multivalent MnO_x according to JCPS databases (a), XRD patterns of MnO_x, C(N), C(N)/ MnO_x-SP, rGO(N), rGO(N)/ MnO_x-SP (b).

Such peaks are shifted toward higher angles as compared to graphene oxide, due to N-dopoping and the reduction of GO to rGO which causes the partial loss of oxygen-containing functional groups (45, 46). According to the diffraction pattern in Fig. 2b, the crystalline structure of manganese oxide remains similar even after the formation of C(N)/ MnO_x-SP and rGO(N)/ MnO_x-SP.

Raman spectroscopy was used to further study the physical properties of the prepared materials (Figure 3). The Raman spectra of MnOx, C(N)/ MnOx-SP, and rGO(N)/ MnOx-SP show a peak at 647 cm^{-1}, 645 cm^{-1}, and 615 cm^{-1}, respectively, due to the asymmetric stretching vibration of Mn-O bonds in the

MnO_x compounds (47). According to previous reports, crystallite size affects position and width of Raman peaks, while the oxygen deficiency does not cause any shift or broadening of Raman peaks (48). The shift toward lower wavenumbers and the broadening of the peak for rGO(N)/ MnO_x-SP can be ascribed to a smaller grain size of this sample as compared to C(N)/ MnOx-SP.

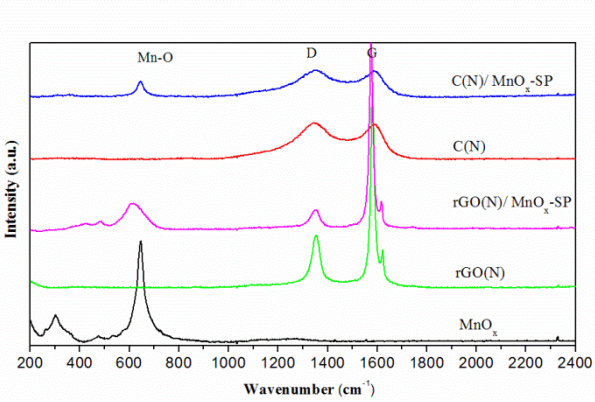

Figure 3-Raman spectra of MnO_x, rGO(N), rGO(N)/ MnO_x-SP, C(N), C(N)/ MnO_x-SP

As indicated in Table 2, Raman spectra of pristine C(N) and rGO(N) displays two distinct peaks ascribed to the D-band (at 1346 cm^{-1} and 1353 cm^{-1}, respectively) and G-band (at 1589 cm^{-1} and 1581 cm^{-1}, respectively). Generally, the appearance of the D band is due to the presence of sp^3 carbons or defect-induced disorder in graphene sheets, and G band results from vibrations of sp^2 carbons (49).

Table 2-Raman parameters for C(N), rGO(N), rGO(N)/ MnO_x-SP, C(N)/ MnO_x-SP, MnO_x.

Samples	**D Band (cm^{-1})**	**G band (cm^{-1})**	**I_D/I_G**	**Mn-O (cm^{-1})**
C(N)	1346	1589	1.00	-
rGO(N)	1353	1581	0.32	-
rGO(N)/ MnO_x-SP	1351	1575	0.32	615.14
C(N)/ MnO_x-SP	1350	1587	1.00	643.27
MnO_x	-	-	-	646.77

The ratio of D to G band intensities (I_D/I_G) is related to the amount of defects in samples. I_D/I_G ratio is higher for C(N)/ MnOx-SP than rGO(N)/ MnOx, indicating that C(N)/ MnOx-SP has a highest degree

of defects. In general, a higher degree of disorder in carbon-based catalysts is related to an enhanced affinity for oxygen adsorption, hence increasing catalytic activity toward ORR (50, 51).

To get insights on surface chemistry and valence states of Mn in nanocrystalline MnO_x, X-ray photoelectron spectroscopy (XPS) was performed. Figure 4 shows N1s and Mn2p XPS spectra of C(N)/ MnO_x-SP, as a representative sample of the series. Nitrogen and manganese peak fitting is also shown in **Errore. L'origine riferimento non è stata trovata.**, and the corresponding results are listed in Table 3.

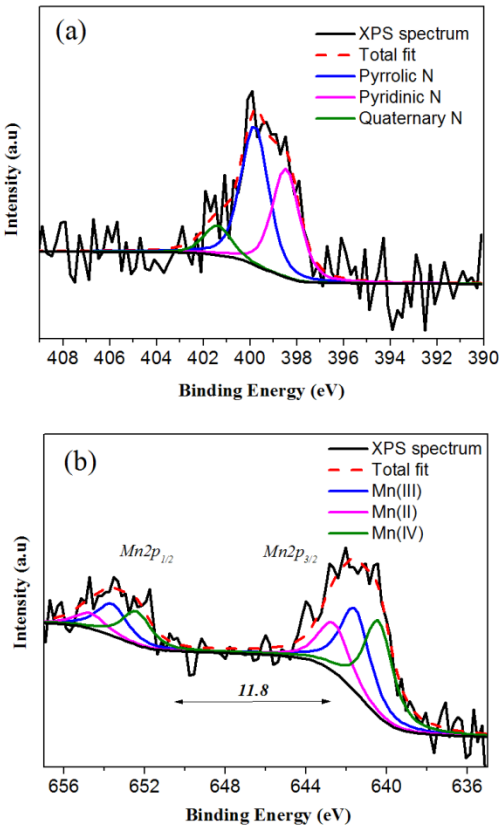

Figure 4- N1s (a) and Mn2p (b) XPS spectra of C(N)/ MnO_x-SP

For N 1s spectrum, the main peak is deconvoluted into three different peaks, centered at 398.4, 399.7, and 400.3 eV, corresponding to pyridinic-N, pyrrolic-N, and quaternary-N, respectively (**Errore. L'origine riferimento non è stata trovata.**a). These results further demonstrate that C(N)/ MnO_x-SP

composite contains nitrogen in the structure. The Mn2p spectrum (**Errore. L'origine riferimento non è stata trovata.**b) shows two principal and typical peaks around 641.6 eV and 653.4 eV which can be attributed to the binding energy of Mn $2p_{3/2}$ and Mn $2p_{1/2}$, respectively. Generally, the XPS peak of Mn $2p_{3/2}$ can be deconvoluted in three different contributions assigned to Mn^{2+} (640.3 eV), Mn^{3+} (641.5 eV) and Mn^{4+} (642.5 eV), respectively. These results confirmed the coexistence of Mn^{+2}, Mn^{+3}, and Mn^{+4}, and thus the presence of Mn_3O_4, Mn_2O_3, MnO and MnO_2 in the synthesized sample as previously shown in the XRD patterns. Comparing the relative intensity of Mn2p peak in table 3, lower valence states (Mn^{2+} and Mn^{3+}) are predominant in C(N)/ MnOx-SP.

Table 3- XPS parameters from N1s and Mn2p peak fitting of C(N)/ MnO_x-SP.

N1s			Mn2p		
N type	Peak BE (eV)	Rel. Intensity%	Mn type	Peak BE (eV)	Rel. Intensity%
Pyridinic-N	398.4	39.6	Mn^{2+}	640.3	40.6
Pyrrolic-N	399.7	49.8	Mn^{3+}	641.5	38.2
Quaternary-N	400.3	10.6	Mn^{4+}	642.5	21.2

CV was used to investigate the electrocatalytic activity of the synthesized nanocatalysts toward ORR in oxygen and nitrogen saturated neutral electrolyte solution. As shown in Fig. 5, upon introduction of O_2 in the electrolyte solution, a reduction peak can be seen for C(N)/ MnO_x-SP and rGO(N)/ MnO_x-SP, as a clear indication that both materials are catalytically active toward ORR.

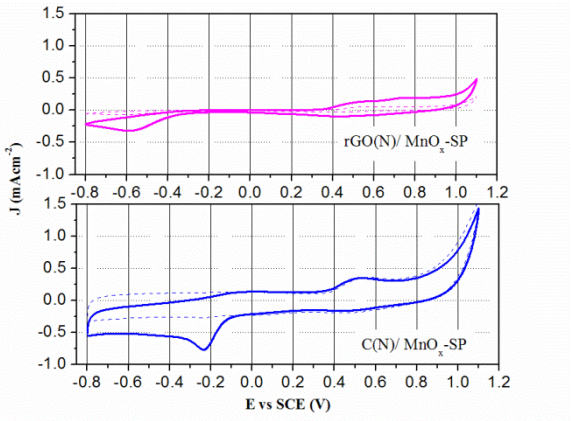

Figure 5- Cyclic voltammograms of rGO(N)/ MnO_x-SP and C(N)/ MnO_x-SP catalysts in N_2- (dashed lines) and O_2-saturated (solid lines) 100 mM neutral PBS solution. Scan rate = 10 mVs^{-1}.

Peak potential values and the corresponding current density values are shown in Table 4. In particular, for C(N)/ MnO_x-SP the reduction peak is shifted towards a more positive potential and peak current density is higher as compared to rGO(N)/ MnO_x-SP due to an enhanced catalytic activity for C(N)/ MnO_x-SP. To further evaluate the catalytic behavior of the prepared samples, the double layer capacitance (C_{DL}) was calculated by acquiring CVs in nitrogen saturated PBS at different scan rates, as previously reported (38), and the results are show in Table 4. Higher C_{DL} values can be associated to higher surface area and density of available active sites (52, 53). Higher C_{DL} values for C(N)/ MnO_x-SP as compared to rGO(N)/MnO_x-SP leads to higher peak current density and more positive potential for ORR.

Table 4- Peak potential, peak current density, and double layer capacitance extrapolated from CVs.

Sample	E_{pr}/V	J_{pr}/$mAcm^{-2}$	C_{DL}/$mFcm^{-2}$
C(N)/ MnO_x-SP	-0.23	-0.77	0.55
rGO(N)/ MnO_x-SP	-0.60	-0.07	0.05

To get deeper insights on the kinetic mechanism of ORR at the surface of the prepared catalysts, we performed RDE experiments at different electrode rotation rates. Fig. 6a and 6b shows LSV curves at electrode rotation rates from 100 to 1600 rpm, for Pt/C (taken as reference) and C(N)/ MnO_x-SP (as a representative sample of the MnO_x-based catalysts).

Data were analyzed with the Koutecky–Levich (KL) theory according to which the measured current is given by eq. 1:

$$\frac{1}{J} = \frac{1}{J_K} + \frac{1}{J_D} \quad (1)$$

where J_K is the kinetic current density and J_D is the limiting current density (eq. 2):

$$J_D = 0.62nFCD^{2/3}\nu^{-1/6}\omega^{1/2} \quad (2)$$

where n is the number of electrons exchanged, F is Faraday's constant, C is oxygen concentration , D is oxygen diffusivity, ν is the kinematic viscosity of the electrolyte, and ω is the electrode rotation rate (54). By plotting the inverse of the measured current density as a function of the inverse of the square root of the rotation rate, KL plots are obtained at E=-0.6 V and shown as an inset of Fig 6a and Fig.6b, and in Fig. 6d for the sake of comparison. KL plots show a good linearity for the two samples which indicates first-order kinetics of ORR. The electrochemical parameters extrapolated from the KL plots, such as the kinetic current density (J_K) and the number of electrons exchanged (n), are listed in Table 5, together with half-wave potential ($E_{1/2}$) values taken from LSVs at 1600 rpm. The data in Table 5 demonstrated that ORR catalyzed by C(N)/ MnO_x-SP mainly proceeds through a 4 electron pathway mechanism, as in the case of reference Pt/C. $E_{1/2}$ of C(N)/ MnO_x-SP is less positive than that of Pt/C and J_K is lower, but those values outperform the performance previously reported for typical MnO_2-based catalysts (55).

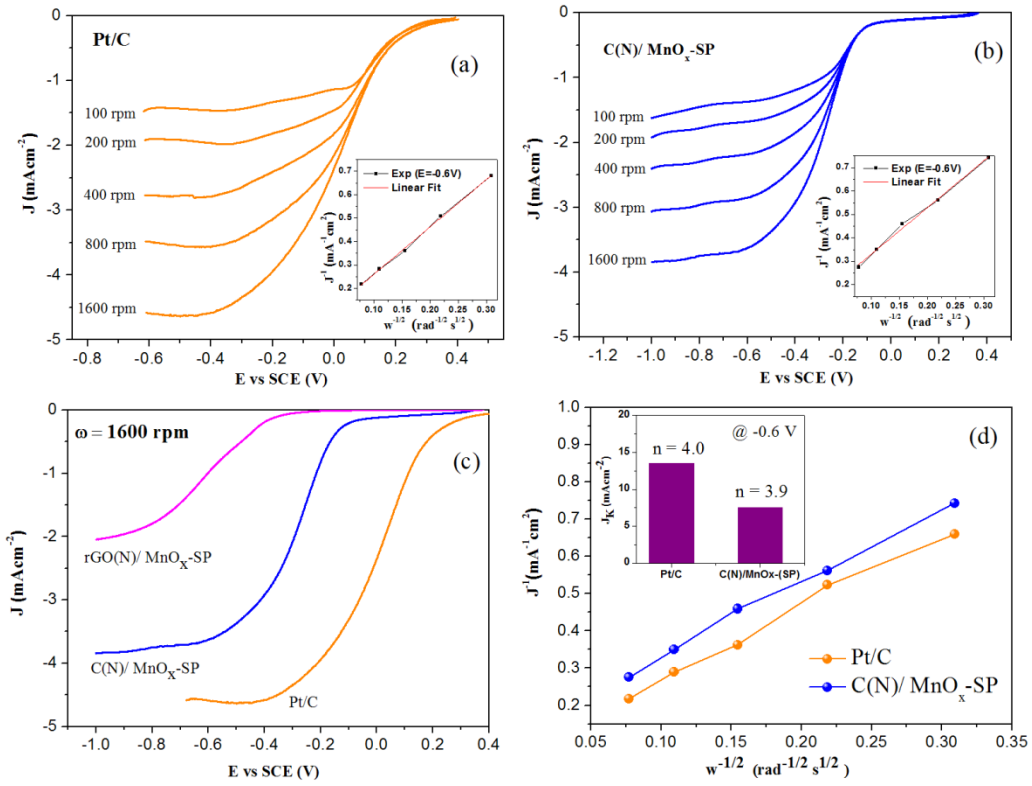

Figure 6- LSV curves at different electrode rotation rates of (a) Pt/C, and (b) C(N)/ MnO_x-SP with KL plots as inset obtained at -0.6 V; c) LSV curves at 1600 rpm of rGO(N)/ MnO_x-SP, C(N)/ MnO_x-SP; d) Comparison of KL plots of C(N)/ MnOx-SP and Pt/C at –0.6 V (Inset: Jk and n @ -0.6 V).

The comparison of LSVs at 1600 rpm for Pt/C, C(N)/ MnO_x-SP, and rGO(N)/MnO_x-SP, shown in Fig. 6c, further confirms that C(N)/ MnO_x-SP performs similarly to Pt/C as ORR catalyst, while the performance of rGO(N)/MnO_x-SP has the worst overall performance.

Table 5- Half-wave potential ($E_{1/2}$), kinetic current density (J_K), and the number of electrons exchanged (n) extracted from LSVs, at 1600 rpm and -0.6 V, respectively.

Sample	**$E_{1/2}$ / V ω=1600 rpm**	**J_K / mAcm^{-2} @ -0.6 V**	**n @ -0.6 V**
Pt/C	-0.02	13.5	4.0
C(N)/ MnOx-SP	-0.28	7.5	3.9

The enhanced ORR performance of C(N)/ MnO_x-SP as compared to rGO(N)/ MnO_x-SP can be further analyzed by EIS analysis. Fig. 7 shows the Nyquist plots of C(N)/ MnO_x-SP and rGO(N)/ MnO_x-SP under static (Fig. 7a) and hydrodynamic (Fig. 7b) conditions. Potentiostatic EIS spectra were obtained at the half-wave potential of LSV curves, as described in 2.2 section (materials characterization).

The spectra shown in Fig. 7a consist of a tail in the low frequency range that is related to diffusion of both oxygen and ionic species through the diffusion layer at the electrode/electrolyte interface. At neutral pH and in static conditions the thickness of the diffusion layer is high, and mass transfer to/from this thick region is hindered. To limit this diffusion layer to a certain extent (finite) and reduce the effect of mass transfer, we carried out EIS under hydrodynamic condition at a electrode rotation rate of 1600 rpm (Fig. 7b). As a result, the diameter of the semicircle at high frequency decreased as compared to the case of Fig. 7a. EIS spectra in Fig. 7b were modeled by using the a Randles-type circuit depicted in Fig. 7c, suitable for modeling finite linear diffusion in heterogeneous materials (56-59). In the circuit model, the elements represent ohmic resistance (R_s), charge transfer resistance (R_{ct}), a constant phase

element related to double layer capacitance (CPE) and a short Warburg element (W_s), related to depressed arcs at low frequencies which tend to intercept the X-axis. According to this model mass diffusion is limited to a finite and narrow layer, while charge transfer plays a predominant role on the overall electrode process (59-61).

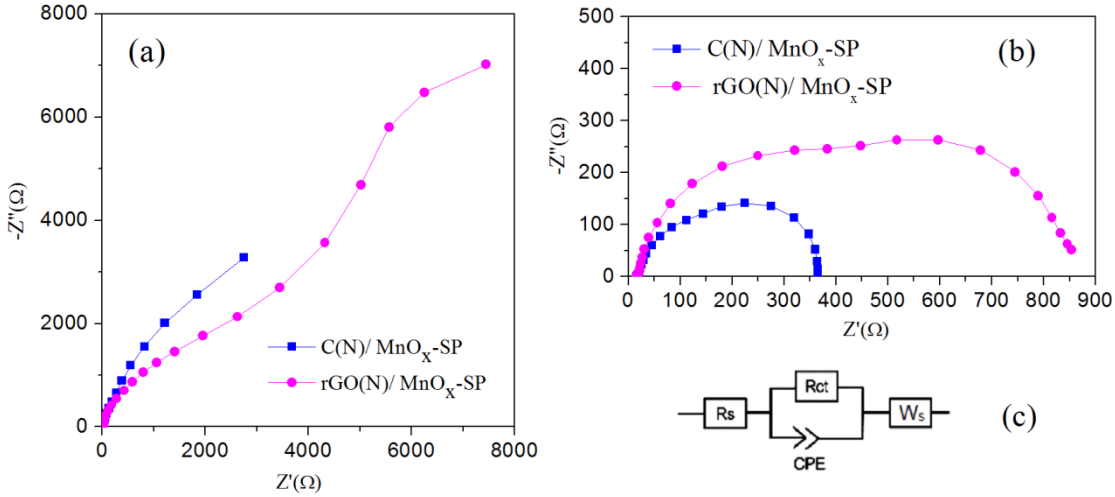

Figure 7. Nyquist plots for C(N)/ MnO_x-SP and rGO(N)/ MnO_x-SP in O_2-saturated neutral PBS a) under static (0 rpm) and b) hydrodynamic (1600 rpm) conditions.

Table 6 shows the fitting results, limited to charge transfer parameters. C_{DL} values were calculated according to eq. 3 (62):

$$C_{DL} = \frac{(R_{CT} \times CPE)^{\frac{1}{\alpha}}}{R_{CT}} \qquad (3)$$

where α is the CPE index, accounting for deviations from ideality.

Table 6. EIS parameters for C(N)/ MnO_x-SP and rGO(N)/ MnO_x-SP (from fitting of EIS spectra at 1600 rpm).

Samples / Parameters	C(N)/ MnO_x-SP	Error %	rGO(N)/ MnO_x-SP	Error %
R_s (Ω)	16.31	0.50	16.23	0.95
R_{ct} (Ω)	292.80	1.96	366.70	4.04

α	0.96	1.53	0.99	1.43
CPE (Ss^{α})	$1.54x10^{-3}$	2.79	$7.90x10^{-5}$	5.23
C_{DL} ($mFcm^{-2}$)	1.39	-	0.08	-

R_S, which accounts for the solution resistance, was the same for both electrodes, while R_{CT} was lower for C(N)/ MnO_x-SP than rGO(N)/MnOx-SP, as a further indication of enhanced ORR for this material, in good agreement with CV and LSV analysis. Also, C_{DL} of C(N)/ MnO_x-SP was higher than that of rGO(N)/MnOx-SP. The higher double layer capacitance can be related to a comprehensive effect of texture and roughness on the electrode surface of C(N)/ MnO_x-SP sample, arising from the nano-structural properties of the materials. Values of CPE index (α) very close to 1 have been previously reported for rough interfaces (63).

C_{DL} values obtained by EIS (hydrodynamic conditions) are higher than those calculated by CV (quiet conditions).This finding can be ascribed to the lower thickness of the double layer in EIS experiments under hydrodynamic conditions, as previously reported (64, 65).

In view of good catalytic activity toward ORR, as elucidated by the materials characterization, C(N)/ MnO_x-SP was selected to be assembled at the air-breathing cathode of a single-chamber MFC, and its performance, in terms of voltage and power generation, was compared to that of a reference Pt/C cathode.

As illustrated in Fig. 8a, in spite of higher open circuit voltage (OCV) of Pt/C (0.71 V) with respect to C(N)/ MnO_x-SP (0.37 V), the maximum power density the MFC assembled with C(N)/ MnO_x-SP is 467 mWm^{-2}, which is higher than that of Pt/C (446 mWm^{-2}). Moreover, C(N)/ MnO-SP also shows higher current density at 0.2 V (2583 mAm^{-2}) than Pt/C (1128 mAm^{-2}), as a further improvement. These results suggest that the overall polarization of C(N)/ MnO_x-SP cathode resulted in enhanced power generation as compared to the Pt/C cathode.

Taking into account different cell configuration and different operative conditions, electricity and power generation are consistent with existing literature reporting the performance of MFCs assembled with cathodes based either on MnOx or PGM-free catalysts (35, 36, 66-68).

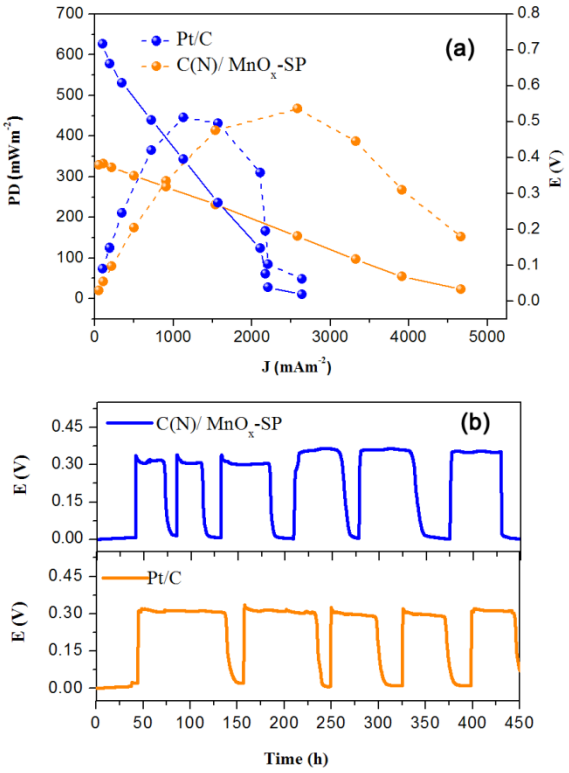

Figure 8- a) Polarization and power density (PD) curves of MFCs assembled with C(N)/ MnO_x-SP and Pt/C cathodes fed with 1mgL^{-1} sodium acetate in neutral phosphate buffer, b) Voltage cycles under a 1 kV external resistance as a function of time.

Stability tests were also performed, by acquiring voltage generation cycles in long-term operation mode. Fig. 8b indicates that both MFCs, assembled with C(N)/ MnO_x-SP and Pt/C as cathode, allowed achieving constant and reproducible voltage cycles, denoting that the C(N)/ MnO_x-SP catalyst has a good stability, being able to generate constant voltage over 450 h working as an MFC cathode.

Additionally, with a rough cost estimation on the basis of a lab-scale procedure for materials synthesis, C(N)/ MnO_x-SP has an average cost of 2 €g^{-1}, which is much lower than the cost of commercial Pt/C (25 €g^{-1}). The joint analysis of performance and costs points at C(N)/ MnO_x-SP as a promising catalyst to replace Pt for MFC application, also considering the possibility of further cost reduction in scaling-up the process of materials synthesis.

4 Conclusions

In this work we developed a novel, facile, and low-cost solid phase synthesis to prepare multivalent MnO_x supported on nitrogen-doped nanostructured carbon as oxygen reducing catalyst. Either nitrogen-doped carbon black (C(N)) or nitrogen-doped reduced graphene oxide (rGO(N)) were selected as carbon support for MnO_x. Among the prepared materials, MnO_x supported on C(N) showed the highest catalytic activity toward the oxygen reduction reaction due to a good combination between surface chemistry and morphology. When assembled at the cathode side of a lab-scale prototype of microbial fuel cells (MFCs), C(N)/ MnO_x-SP generated high electrical power and stable voltage, outperforming commercial Pt/C cathode, taken as the reference catalyst. Hence, this catalyst can be identified as an appropriate alternative to Pt-based cathode for MFC applications.

Acknowledgements

The present work was carried out with the financial support of the Post Graduate Office of the University of Tabriz and the CNPq - Conselho Nacional de Desenvolvimento Científico e Tecnologico, Brazil, under the grant n.200631 - 2015/2. Also, the valuable technical support of Mrs. C. D'Ottavi is gratefully acknowledged.

5 References

1. Zhang X, He W, Ren L, Stager J, Evans PJ, Logan BE. COD removal characteristics in air-cathode microbial fuel cells. Bioresource technology. 2015;176:23-31.
2. Rinaldi A, Mecheri B, Garavaglia V, Licoccia S, Di Nardo P, Traversa E. Engineering materials and biology to boost performance of microbial fuel cells: a critical review. Energy & Environmental Science. 2008;1(4):417-29.
3. Santoro C, Arbizzani C, Erable B, Ieropoulos I. Microbial fuel cells: From fundamentals to applications. A review. Journal of Power Sources. 2017;356:225-44.
4. Midyurova B, Yemendzhiev H, Tanev P, Nenov V. Application of Ceramic Materials to the Microbial Fuel Cell Design. Journal of Chemical Technology & Metallurgy. 2015;50(4).
5. Kong F, Longo RC, Zhang H, Liang C, Zheng Y, Cho K. Charge-transfer modified embedded-atom method for manganese oxides: Nanostructuring effects on MnO 2 nanorods. Computational Materials Science. 2016;121:191-203.
6. Wen Q, Wang S, Yan J, Cong L, Pan Z, Ren Y, et al. MnO 2–graphene hybrid as an alternative cathodic catalyst to platinum in microbial fuel cells. Journal of power sources. 2012;216:187-91.
7. Chin C-C, Yang H-K, Chen J-S. Investigation of MnO2 and ordered mesoporous carbon composites as electrocatalysts for Li-O2 battery applications. Nanomaterials. 2016;6(1):21.
8. Wang Y, Zhong H, Hu L, Yan N, Hu H, Chen Q. Manganese hexacyanoferrate/MnO 2 composite nanostructures as a cathode material for supercapacitors. Journal of Materials Chemistry A. 2013;1(7):2621-30.
9. Kumari V, Tripathi B, Dixit A. beta phase manganese dioxide nanorods Synthesis and characterization for supercapacitor applications. arXiv preprint arXiv:151000802. 2015.
10. Li X, Hu B, Suib S, Lei Y, Li B. Manganese dioxide as a new cathode catalyst in microbial fuel cells. Journal of Power Sources. 2010;195(9):2586-91.
11. Rafique A, Massa A, Fontana M, Bianco S, Chiodoni A, Pirri CF, et al. Highly Uniform Anodically Deposited Film of MnO2 Nanoflakes on Carbon Fibers for Flexible and Wearable Fiber-Shaped Supercapacitors. ACS applied materials & interfaces. 2017;9(34):28386-93.
12. Rao C, Vivekchand S, Biswas K, Govindaraj A. Synthesis of inorganic nanomaterials. Dalton Transactions. 2007(34):3728-49.
13. Delmondo L, Salvador GP, Muñoz-Tabares JA, Sacco A, Garino N, Castellino M, et al. Nanostructured Mn x O y for oxygen reduction reaction (ORR) catalysts. Applied Surface Science. 2016;388:631-9.
14. Delmondo L, Muñoz-Tabares JA, Sacco A, Garino N, Massaglia G, Castellino M, et al. Thermal evolution of Mn x O y nanofibres as catalysts for the oxygen reduction reaction. Physical Chemistry Chemical Physics. 2017;19(42):28781-7.
15. Suib SL. Porous manganese oxide octahedral molecular sieves and octahedral layered materials. Accounts of chemical research. 2008;41(4):479-87.
16. Suib SL. Structure, porosity, and redox in porous manganese oxide octahedral layer and molecular sieve materials. Journal of Materials Chemistry. 2008;18(14):1623-31.
17. Cheng F, Su Y, Liang J, Tao Z, Chen J. MnO2-based nanostructures as catalysts for electrochemical oxygen reduction in alkaline media. Chemistry of Materials. 2009;22(3):898-905.
18. Devaraj S, Munichandraiah N. Effect of crystallographic structure of MnO2 on its electrochemical capacitance properties. The Journal of Physical Chemistry C. 2008;112(11):4406-17.
19. Bergmann A, Zaharieva I, Dau H, Strasser P. Electrochemical water splitting by layered and 3D cross-linked manganese oxides: correlating structural motifs and catalytic activity. Energy & Environmental Science. 2013;6(9):2745-55.
20. Thackeray MM. Manganese oxides for lithium batteries. Progress in Solid State Chemistry. 1997;25(1):1-71.

21. Le MLP. Nanostructured composite electrode based on manganese dioxide and carbon vulcan–carbon nanotubes for an electrochemical supercapacitor. Advances in Natural Sciences: Nanoscience and Nanotechnology. 2013;4(3):035004.
22. Awan Z, Nahm KS, Xavier JS. Nanotubular MnO 2/graphene oxide composites for the application of open air-breathing cathode microbial fuel cells. Biosensors and Bioelectronics. 2014;53:528-34.
23. Zeng D, Yu X, Zhan Y, Cao L, Wu X, Zhang B, et al. Insight into the nitrogen-doped carbon as oxygen reduction reaction catalyst: The choice of carbon/nitrogen source and active sites. International Journal of Hydrogen Energy. 2016;41(20):8563-75.
24. Wang H, Maiyalagan T, Wang X. Review on recent progress in nitrogen-doped graphene: synthesis, characterization, and its potential applications. Acs Catalysis. 2012;2(5):781-94.
25. Yao Y, Zhang B, Shi J, Yang Q. Preparation of nitrogen-doped carbon nanotubes with different morphologies from melamine-formaldehyde resin. ACS applied materials & interfaces. 2015;7(13):7413-20.
26. Maldonado S, Stevenson KJ. Influence of nitrogen doping on oxygen reduction electrocatalysis at carbon nanofiber electrodes. The Journal of Physical Chemistry B. 2005;109(10):4707-16.
27. Santoro C, Gokhale R, Mecheri B, D'Epifanio A, Licoccia S, Serov A, et al. Design of Iron (II) Pthalocyanine (FePc) Derived Oxygen Reduction Electrocatalysts for High Power Density Microbial Fuel Cells. ChemSusChem.
28. Erable B, Féron D, Bergel A. Microbial catalysis of the oxygen reduction reaction for microbial fuel cells: a review. ChemSusChem. 2012;5(6):975-87.
29. Daems N, Sheng X, Vankelecom IF, Pescarmona PP. Metal-free doped carbon materials as electrocatalysts for the oxygen reduction reaction. Journal of Materials Chemistry A. 2014;2(12):4085-110.
30. Ferrero GA, Fuertes AB, Sevilla M, Titirici M-M. Efficient metal-free N-doped mesoporous carbon catalysts for ORR by a template-free approach. Carbon. 2016;106:179-87.
31. Lu M, Kharkwal S, Ng HY, Li SFY. Carbon nanotube supported MnO 2 catalysts for oxygen reduction reaction and their applications in microbial fuel cells. Biosensors and Bioelectronics. 2011;26(12):4728-32.
32. Zhang P, Li K, Liu X. Carnation-like MnO 2 modified activated carbon air cathode improve power generation in microbial fuel cells. Journal of Power Sources. 2014;264:248-53.
33. Gautam RK, Bhattacharjee H, Mohan SV, Verma A. Nitrogen doped graphene supported α-MnO 2 nanorods for efficient ORR in a microbial fuel cell. RSC Advances. 2016;6(111):110091-101.
34. Li X, Hu B, Suib S, Lei Y, Li B. Electricity generation in continuous flow microbial fuel cells (MFCs) with manganese dioxide (MnO 2) cathodes. Biochemical Engineering Journal. 2011;54(1):10-5.
35. Burkitt R, Whiffen T, Yu EH. Iron phthalocyanine and MnOx composite catalysts for microbial fuel cell applications. Applied Catalysis B: Environmental. 2016;181:279-88.
36. Tiwari B, Noori MT, Ghangrekar M. Carbon supported nickel-phthalocyanine/MnOx as novel cathode catalyst for microbial fuel cell application. International Journal of Hydrogen Energy. 2017;42(36):23085-94.
37. Iannaci A, Mecheri B, D'Epifanio A, Elorri MJL, Licoccia S. Iron–nitrogen-functionalized carbon as efficient oxygen reduction reaction electrocatalyst in microbial fuel cells. International Journal of Hydrogen Energy. 2016;41(43):19637-44.
38. de Oliveira MAC, Mecheri B, D'Epifanio A, Placidi E, Arciprete F, Valentini F, et al. Graphene oxide nanoplatforms to enhance catalytic performance of iron phthalocyanine for oxygen reduction reaction in bioelectrochemical systems. Journal of Power Sources. 2017;356:381-8.

39. Iannaci A, Sciarria TP, Mecheri B, Adani F, Licoccia S, D'Epifanio A. Power generation using a low-cost sulfated zirconium oxide based cathode in single chamber microbial fuel cells. Journal of Alloys and Compounds. 2017;693:170-6.
40. Sciarria TP, Merlino G, Scaglia B, D'Epifanio A, Mecheri B, Borin S, et al. Electricity generation using white and red wine lees in air cathode microbial fuel cells. Journal of Power Sources. 2015;274:393-9.
41. Nguyen M-T, Mecheri B, D'Epifanio A, Sciarria TP, Adani F, Licoccia S. Iron chelates as low-cost and effective electrocatalyst for oxygen reduction reaction in microbial fuel cells. International Journal of Hydrogen Energy. 2014;39(12):6462-9.
42. Wang L, Huang B, Su Y, Zhou G, Wang K, Luo H, et al. Manganese oxides supported on multi-walled carbon nanotubes for selective catalytic reduction of NO with NH 3: Catalytic activity and characterization. Chemical Engineering Journal. 2012;192:232-41.
43. Tang X, Li Y, Huang X, Xu Y, Zhu H, Wang J, et al. MnO x–CeO 2 mixed oxide catalysts for complete oxidation of formaldehyde: effect of preparation method and calcination temperature. Applied Catalysis B: Environmental. 2006;62(3):265-73.
44. Qi G, Yang RT. Characterization and FTIR Studies of MnO x− CeO2 Catalyst for Low-Temperature Selective Catalytic Reduction of NO with NH3. The Journal of Physical Chemistry B. 2004;108(40):15738-47.
45. Li D, Yu C, Wang M, Zhang Y, Pan C. Synthesis of nitrogen doped graphene from graphene oxide within an ammonia flame for high performance supercapacitors. RSC Advances. 2014;4(98):55394-9.
46. Mishra SK, Tripathi SN, Choudhary V, Gupta BD. SPR based fibre optic ammonia gas sensor utilizing nanocomposite film of PMMA/reduced graphene oxide prepared by in situ polymerization. Sensors and Actuators B: Chemical. 2014;199:190-200.
47. Kar P, Sardar S, Ghosh S, Parida MR, Liu B, Mohammed OF, et al. Nano surface engineering of Mn 2 O 3 for potential light-harvesting application. Journal of Materials Chemistry C. 2015;3(31):8200-11.
48. Zuo J, Xu C, Liu Y, Qian Y. Crystallite size effects on the Raman spectra of Mn3O4. Nanostructured materials. 1998;10(8):1331-5.
49. Ferrari AC, Robertson J. Interpretation of Raman spectra of disordered and amorphous carbon. Physical review B. 2000;61(20):14095.
50. Dubale AA, Su W-N, Tamirat AG, Pan C-J, Aragaw BA, Chen H-M, et al. The synergetic effect of graphene on Cu 2 O nanowire arrays as a highly efficient hydrogen evolution photocathode in water splitting. Journal of Materials Chemistry A. 2014;2(43):18383-97.
51. Liao L, Fang P, Pan C. Nitrogen-doped carbon nanotubes from amine flames. Journal of nanoscience and nanotechnology. 2011;11(2):1060-7.
52. Mecheri B, Iannaci A, D'Epifanio A, Mauri A, Licoccia S. Carbon-Supported Zirconium Oxide as a Cathode for Microbial Fuel Cell Applications. ChemPlusChem. 2016;81(1):80-5.
53. Santoro C, Kodali M, Kabir S, Soavi F, Serov A, Atanassov P. Three-dimensional graphene nanosheets as cathode catalysts in standard and supercapacitive microbial fuel cell. Journal of Power Sources. 2017;356:371-80.
54. Nguyen M-T, Mecheri B, Iannaci A, D'Epifanio A, Licoccia S. Iron/polyindole-based electrocatalysts to enhance oxygen reduction in microbial fuel cells. Electrochimica Acta. 2016;190:388-95.
55. Yuan H, Deng L, Qi Y, Kobayashi N, Hasatani M. Morphology-dependent performance of nanostructured MnO2 as an oxygen reduction catalyst in microbial fuel cells. International Journal Of Electrochemical Science. 2015;10(5):3693-706.

56. Diard J, Le Gorrec B, Montella C. Electrical circuits containing CPEs. Handbook of Electrochemical Impedance Spectroscopy: BioLogic SAS Insturments France; 2013.
57. Bard AJ. LR Faulkner Electrochemical Methods. Wiley, New York; 1980.
58. Quevedo MC, Galicia G, Mayen-Mondragon R, Llongueras JG. Role of turbulent flow seawater in the corrosion enhancement of an Al–Zn–Mg alloy: an electrochemical impedance spectroscopy (EIS) analysis of oxygen reduction reaction (ORR). Journal of Materials Research and Technology. 2017.
59. Boillot M, Didierjean S, Lapicque F. Impedance of a rotating disc electrode with a reversible reaction. Journal of applied electrochemistry. 2004;34(12):1191-7.
60. Macdonald JR, Barsoukov E. Impedance spectroscopy: theory, experiment, and applications. History. 2005;1(8).
61. Fu Y, Poizeau S, Bertei A, Qi C, Mohanram A, Pietras J, et al. Heterogeneous electrocatalysis in porous cathodes of solid oxide fuel cells. Electrochimica Acta. 2015;159:71-80.
62. Hidalgo D, Sacco A, Hernández S, Tommasi T. Electrochemical and impedance characterization of Microbial Fuel Cells based on 2D and 3D anodic electrodes working with seawater microorganisms under continuous operation. Bioresource technology. 2015;195:139-46.
63. Córdoba-Torres P, Mesquita TJ, Nogueira RP. Relationship between the origin of constant-phase element behavior in electrochemical impedance spectroscopy and electrode surface structure. The Journal of Physical Chemistry C. 2015;119(8):4136-47.
64. Qu D, Shi H. Studies of activated carbons used in double-layer capacitors. Journal of Power Sources. 1998;74(1):99-107.
65. Zhang S, Pan N. Supercapacitors performance evaluation. Advanced Energy Materials. 2015;5(6).
66. Santoro C, Serov A, Narvaez Villarrubia CW, Stariha S, Babanova S, Schuler AJ, et al. Double-Chamber Microbial Fuel Cell with a Non-Platinum-Group Metal Fe–N–C Cathode Catalyst. ChemSusChem. 2015;8(5):828-34.
67. Kodali M, Santoro C, Serov A, Kabir S, Artyushkova K, Matanovic I, et al. Air breathing cathodes for microbial fuel cell using Mn-, Fe-, Co-and Ni-containing platinum group metal-free catalysts. Electrochimica acta. 2017;231:115-24.
68. Kodali M, Gokhale R, Santoro C, Serov A, Artyushkova K, Atanassov P. High Performance Platinum Group Metal-Free Cathode Catalysts for Microbial Fuel Cell (MFC). Journal of The Electrochemical Society. 2017;164(3):H3041-H6.